Dissipationless Circulating Currents and Fringe Magnetic Fields Near a Single Spin Embedded in a Two-Dimensional Electron Gas

Adonai R. da Cruz[1,*] and Michael E. Flatté[2,1,†]

[1]*Department of Applied Physics, Eindhoven University of Technology, Eindhoven 5612 AZ, The Netherlands*
[2]*Department of Physics and Astronomy, University of Iowa, Iowa City, Iowa 52242, USA*

Theoretical calculations predict the anisotropic dissipationless circulating current induced by a spin defect in a two-dimensional electron gas. The shape and spatial extent of these dissipationless circulating currents depend dramatically on the relative strengths of spin-orbit fields with differing spatial symmetry, offering the potential to use an electric gate to manipulate nanoscale magnetic fields and couple magnetic defects. The spatial structure of the magnetic field produced by this current is calculated and provides a direct way to measure the spin-orbit fields of the host, as well as the defect spin orientation, e.g., through scanning nanoscale magnetometry.

Single spins associated with point defects in solid-state materials are promising candidates for qubits and novel quantum spintronic devices for communication, sensing, and information processing [1–5]. Isolated magnetic dopants embedded in two-dimensional electron gases (2DEGs) with spin-orbit coupling (SOC) can be electrically and optically addressed [6–8] and coherently manipulated. Control of the relative phases of defect spin wave functions through manipulation of the spin-spin coupling enables spin-based quantum computation [1–3]. To date most spin-spin couplings are achieved either through dipolar magnetic fields arising from the spin [9,10], which are difficult to tune, or through photonic coupling [11], which is effective for much longer distances. The magnetic moment of a bare spin is modified by the spin-orbit interaction of the host, leading to proposals for single-spin control via g tensor manipulation [12–19], however, the effects on nanoscale dipolar fields and the consequences for coupling spins remain unexplored.

Here we derive the dissipationless circulating current surrounding a spin embedded in a 2DEG with spin-orbit coupling, and show that these effects are significant and their anisotropic spatial structure is detectable by current nanoscale magnetometry [20–23]. The spin-orbit interaction in a 2DEG can be modified with a perpendicular electric field (without dissipative current flow) thus we further propose that modifying these magnetic fields provides a method of electrically tuning spin-spin interactions to produce quantum entangling gates. Our results rely on a derivation of the 2DEG's current operator that identifies the critical role of effective spin-orbit vector potentials in correctly producing currents that are dissipationless. We compare diverse hosts for these phenomena including semiconductor quantum wells (QWs) and surfaces (e.g., the electron accumulation layer in InAs [24–26]),

oxide interfaces (e.g., $LaAlO_3/SrTiO_3$ [27]), atomically thin materials (e.g., BiSb [28] and WSeTe [29]) and films (e.g., $LaOBiS_2$ [30]). Our expressions for circulating currents connect to other fundamental features of an electron gas interacting with localized magnetic moments, including Friedel oscillations of charge and spin densities [31,32], the Dzyaloshinskii-Moriya interaction [33], and long-range Ruderman-Kittel-Kasuya-Yosida (RKKY) [34–37] interactions between defects. Measurement of the spatial structure of this current can be achieved by probing the magnetic fringe field above the surface with nanoscale scanning magnetometry [e.g., using nitrogen-vacancy (NV) centers in diamond [20–23]], which have achieved spatial resolution in the nanometer range and field sensitivity (tens to hundreds of nT), on the order of the features calculated here. Another option relies on recent advances in electron ptychography for direct sensing [38].

Central to our results is the derivation of the current operator associated with the effective Hamiltonian describing a 2DEG with SOC in a noncentrosymmetric material,

$$H = \frac{\hbar^2 k^2}{2m^*} + \alpha(\sigma_x k_y - \sigma_y k_x) + \beta(\sigma_x k_x - \sigma_y k_y). \quad (1)$$

The spin-orbit fields linear in crystal momentum **k** emerge from both the crystal's bulk inversion asymmetry (BIA, with coefficient β) [39] and the inversion asymmetry of the heterostructure (SIA, with coefficient α, which can be tuned by applied electric fields perpendicular to the 2DEG plane) [40]. We derive the current operator (see Supplemental Material [41]) from the steady-state continuity equation $\partial_t n + \nabla \cdot \mathbf{j} = 0$ and group the spin-orbit terms together in an effective spin-dependent vector potential $\mathbf{A}_{so}$. The expected value of the charge current is evaluated using the Green's function (GF) scattering formalism,

$$\mathbf{j}(\mathbf{r}) = -\frac{e\hbar}{2\pi m^*}\,\mathrm{Im}\int_{E_{so}}^{E_f}(t_\uparrow - t_\downarrow)\left\{i[(\nabla G^0_{\uparrow\downarrow})G^0_{\downarrow\uparrow} - (\nabla G^0_{\downarrow\uparrow})G^0_{\uparrow\downarrow}] - \frac{2e}{\hbar}(\mathbf{A}^{\uparrow\downarrow}_{so}G^0_{\downarrow\uparrow} - \mathbf{A}^{\downarrow\uparrow}_{so}G^0_{\uparrow\downarrow})G^0_{\uparrow\uparrow}\right\}dE, \qquad (2)$$

where $G^0(\mathbf{r},\mathbf{r}')$ are the 2DEG retarded GFs, t_σ are the defect T-matrix elements with spin projection σ, E_{so} is the energy minimum of the 2DEG, E_f is the Fermi energy (determined by the electron density n), and the effective vector potential

$$\mathbf{A}_{so} = \frac{\hbar k_{so}}{e}\{[\sigma_x\cos(\theta-\tau) - \sigma_y\sin(\theta+\tau)]\hat{r} \\ + [\sigma_x\sin(\theta-\tau) - \sigma_y\cos(\theta+\tau)]\hat{\theta}\}, \qquad (3)$$

with $\tau = \tan^{-1}(\alpha/\beta)$ and $k_{so} = (m^*/\hbar^2)\sqrt{\alpha^2+\beta^2}$.

The retarded Green's function from Eq. (1) is [43]

$$g^0(\mathbf{k};E) = \left(\frac{2m^*}{\hbar^2}\right)\frac{(k_E^2-k^2)\sigma_0 - 2k_{so}k[U_x\sigma_x - U_y\sigma_y]}{k_E^4 - 2k^2[k_E^2 + 2k_{so}^2 f_\tau(\theta_k)] + k^4} \qquad (4)$$

where $k_E^2 = 2m^*E/\hbar^2$ and $f_\tau(\theta_k) = 1 + \sin(2\tau)\sin(2\theta_k)$. The poles of the Green's function correspond to Fermi contours of the two spin-split subbands at energy E and are obtained from the roots of the denominator,

$$k_\pm = Q \pm k_{so}\sqrt{f_\tau(\theta_k)}, \qquad Q = \sqrt{k_E^2 + k_{so}^2 f_\tau(\theta_k)}. \qquad (5)$$

The representation of the GF in real space is obtained by Fourier transform of Eq. (4),

$$G^0(\mathbf{r};E) = -\frac{m^*}{2\pi^2\hbar^2}\int_{\theta-\pi/2}^{\theta+\pi/2}d\theta_k\left\{\frac{\sigma_0}{Q}[k_+I_1(k_+\rho) + k_-I_1(k_-\rho)] - i\frac{[U_x\sigma_x - U_y\sigma_y]}{Q\sqrt{f_\tau}}[k_+I_2(k_+\rho) - k_-I_2(k_-\rho)]\right\}, \qquad (6)$$

where $\rho = r\cos(\theta_k - \theta)$, $U_x = \cos(\theta_k - \tau)$, $U_y = \sin(\theta_k + \tau)$, and $I_{1/2}(k_\pm\rho)$ are closed-form functions [43]. Changes in the convexity of the outer contour, $k_+(\theta_k,\tau)$, for a given energy $E = \hbar^2 k_E^2/2m^*$, are driven by the SOC ratio τ through $f_\tau(\theta_k)$ and produce important consequences for electronic properties in real space, such as enhanced electron beam formation for transport along symmetry axes [43].

We now embed a defect with spin employing the Dyson equation for the new GF perturbed by a magnetic potential. For simplicity we assume a δ-function scattering potential centered at the defect position, although our treatment is easily generalized to more complex situations. At low energies, the electron wavelength is much larger than the effective size of the target potential. Taking the lowest order in the partial wave expansion (s-wave approximation), the T matrix assumes the form [44],

$$t_\sigma = \left(\frac{4i\hbar^2}{m^*}\right)[e^{(2i\delta_\sigma)} - 1], \qquad (7)$$

where the scattering phase shift of the spin channel σ, δ_σ, is related to the defect local density of states (LDOS) through the Friedel sum rule [31] and encodes its charge and spin state. This appears in the Dyson equation via

$$\mathbf{G}(\mathbf{r},\mathbf{r}';E) = \mathbf{G}^0(\mathbf{r},0;E)\mathbf{T}\mathbf{G}^0(0,\mathbf{r}';E), \qquad (8)$$

where $\mathbf{G}(\mathbf{r},\mathbf{r}';E)$ is the GF for the system with the defect.

Here we assume an energy independent T matrix for a spin-polarized defect with magnetization fixed along the out-of-plane axis (z axis) where the spin-down state is fully occupied with a LDOS peak below the Fermi energy and thus the spin-down electrons do not participate in scattering processes ($\delta_\downarrow = 0$) while the spin-up channel has a LDOS peak centered at the Fermi energy, and $\delta_\uparrow = \pi/2$.

We now show results for a 2DEG formed by the electron accumulation layer at a InAs(001) surface [24] using $k_{so} = 0.2$ nm^{-1}, $E_f = 10$ meV, and $m^* = 0.023m_0$. The low effective mass, strong spin-orbit coupling, and high Landé g factor makes this a promising system in which to detect these orbital features since the current magnitude is proportional to $(\alpha^2+\beta^2)^{1/2}/m^*$ [Eq. (2)]. Dimensionless scaling factors for different materials are provided in Table I

TABLE I. For several different materials, the parameters (effective mass m^* and spin-orbit strength α) and the scaling factors for the spatial dimension (d_{fac}) and magnetic field strength (B_{fac}) of the features relative to the values for InAs ($d_{\mathrm{fac}} = B_{\mathrm{fac}} = 1$). We assume the QW width is 10 nm.

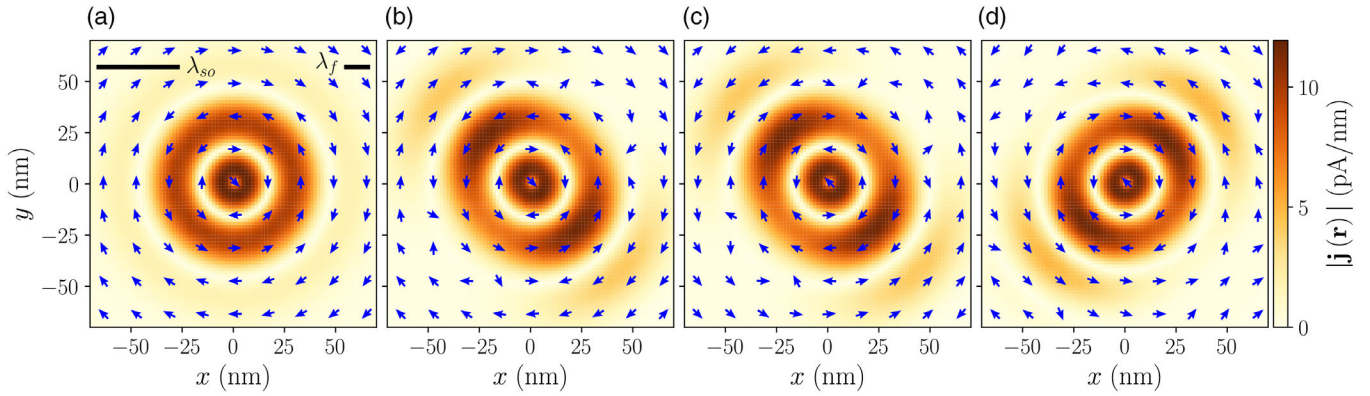| Material	$m^*(m_0)$	α (meV nm)	d_{fac}	B_{fac}
InAs [45]	0.023	50	1.0	1.0
GaAs/AlGaAs [46]	0.067	4.8	3.58	0.096
LAO/STO [27]	2.2	3.4	0.15	0.068
InGaAs/InAlAs [47]	0.05	40.0	0.57	0.8
BiSb [28]	0.002	230	2.5	4.6
LaOBiS$_2$ [30]	0.07	478	0.034	9.56
WSeTe [29,48]	0.81	92	0.015	1.84

FIG. 1. Current density induced by a magnetic point defect with spin pointing perpendicular to an InAs 2DEG. (a) SIA dominated regime ($\beta = 0$, $\tau = \pi/2$) showing angular symmetry. (b)–(d) $\beta \neq 0$; the angularly anistropic circulating current stretches along the symmetry axis $\theta = 3\pi/4$ for $\alpha/\beta > 0$ [(b),(c)] or along $\theta = \pi/4$ for $\alpha/\beta < 0$ (d). Opposite circulation direction of $\tau = \pi/4 + 0.1$ (b) from $\tau = \pi/4 - 0.1$ (c); current vanishes for $\tau = \pi/4$ ($\alpha = \beta$).

for the spatial dimensions (d_{fac}) and for the magnetic field strengths (B_{fac}) in the figures below.

Figure 1 shows the current density induced by a magnetic defect at the origin ($\mathbf{r}_0 = 0$) with spin projection along the [001] out-of-plane direction, calculated from Eq. (2). For $\alpha \gg \beta$, corresponding to $\tau = \pi/2$ (taking the limit $\beta \to 0$ in the definition of τ) [Fig. 1(a)], the isotropic dispersion relation implied by a θ_k-independent f_τ allows for an analytical solution to Eq. (6) in terms of Hankel functions of the first kind [32,49]. The current then has only an angular component and oscillates with two characteristic lengths, reminiscent of Friedel oscillations, given by $\lambda_f = 1/k_f$, tuned by the Fermi energy through charge carrier density and $\lambda_{so} = 1/k_{so}$ which is induced by SOC and is inversely proportional to the applied bias field.

The emergence of the anisotropy in the dispersion relation when both α and β are relevant [Figs. 1(b) and 1(c)] drastically changes the spatial structure of the circulating current compared to Fig. 1(a), stretching the features along the symmetry axes. For $\alpha/\beta > 0$ a stronger current density focuses along the $\theta = 3\pi/4$ direction [Fig. 1(b)] and rotates by 90° focusing along $\theta = \pi/4$ when $\alpha/\beta < 0$ [Fig. 1(c)], a consequence of an interfering contribution of stationary points [43]. The currents are equal but rotate in opposite directions for values of $\tau = \pi/4 \pm \delta$ ($\tau = \pi/4$ corresponds to $\alpha = \beta$), as shown in Figs. 1(b) and 1(c). This change in rotation would invert the orbital magnetization around the spin (see Supplemental Material [41]). We note that when $\alpha = \beta$, the extra SU(2) symmetry implies a fixed spin quantization axis independent of $\mathbf{k}$, making the 2DEG GF of Eq. (6) spin diagonal upon a global spin rotation [50] and thus both contributions to the current in Eq. (2) vanish.

The spatial structure of the orbital magnetization density associated with these circulating currents can be calculated in analogy with classical electrodynamics using [51]

$\mathbf{m}_{\text{orb}}(\mathbf{r}) = (1/2)\mathbf{r} \times \mathbf{j}(\mathbf{r})$; the current density is obtained from Eq. (2). To compare both the orbital and spin contributions to the defect-induced magnetization we calculate the latter by

$$\mathbf{m}_{\text{spin}}(\mathbf{r}) = -\frac{\mu_B}{\pi} \text{Im} \int_{E_{so}}^{E_f} \boldsymbol{\sigma} G(\mathbf{r}; E) dE, \qquad (9)$$

where μ_B is the Bohr magneton and $\boldsymbol{\sigma}$ are the Pauli matrices. We note that orbital momentum quenching is reduced for systems with strong spin-orbit coupling, allowing a comparable orbital magnetization to the spin magnetization. As shown in Fig. 2, although the spin-orbit fields alter both orbital and spin magnetization densities around a magnetic defect, the orbital magnetization has distinct spatial oscillations and is highly sensitive to the SOC ratio τ.

The magnetic fringe field above the 2DEG is obtained from the orbital magnetization density of a quantum well
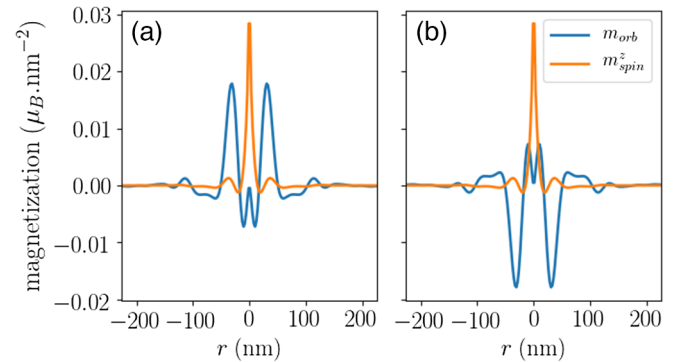

FIG. 2. Orbital (m_{orb}) and spin (m_{spin}^z) contributions to the 2DEG magnetization density showing the effects of the current circulation inversion between $\tau = \pi/4 - 0.1$ (a) and $\tau = \pi/4 + 0.1$ (b) along the [$1\bar{1}0$] direction from a magnetic defect pointing perpendicular to the 2DEG.
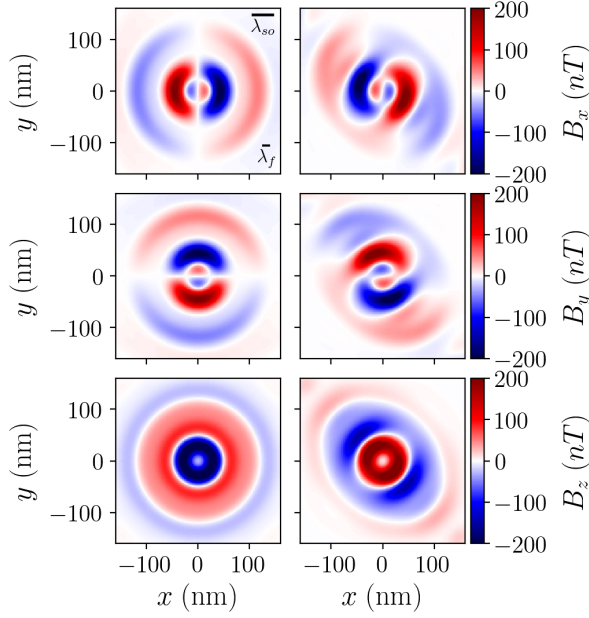
FIG. 3. Orbital fringe field components (a),(b) B_x, (c),(d) B_y, and (e),(f) B_z, 20 nm above the surface of an InAs quantum well with width 10 nm for a magnetic defect pointing perpendicular to the 2DEG. (a),(c),(e) The SIA dominated regime, $\tau = \pi/2$. (b), (d),(f) for $\tau = \pi/8$. The characteristic lengths, λ_f and λ_{so}, are the same from (a) to (f).

FIG. 4. Maximum magnitude of the orbital fringe field components B_x, B_y, and B_z and total magnetic field B calculated at different distances above a 10 nm InAs QW. Shown for $\beta = 0$, $\tau = \pi/2$ (crosses and blue lines) $\beta \neq 0$, $\tau = \pi/8$ (circles and orange lines).

with width d confined along the z axis under hard-wall boundary conditions. By using the ground-state electron envelope function, $\phi(z) = (1/\sqrt{d})\cos(\pi z/d)$, the previously calculated two-dimensional current density acquires a z dependence of $\cos^2(\pi z/d)$, and a volumetric orbital magnetization density can be defined inside the quantum well.

In the region outside the magnetized volume, the magnetic fringe field is evaluated by $\mathbf{B} = -\mu_0 \nabla \Phi_{\text{orb}}(\mathbf{r})$, where $\mu_0 = 4\pi \times 10^{-7}$ N/A^2 is the vacuum permeability and the scalar magnetic potential is [51]

$$\Phi_{\text{orb}}(\mathbf{r}) = \frac{1}{4\pi} \int d\mathbf{r}' \frac{\nabla \cdot \mathbf{m}_{\text{orb}}(\mathbf{r}')}{|\mathbf{r} - \mathbf{r}'|}. \qquad (10)$$

Figure 3 shows the spatial distribution for each orbital fringe field component calculated at 20 nm above a 10 nm InAs QW for this magnetic defect. The largest values are tenths of μT, within the range of single NV diamond scanning magnetometry. In the left column [Figs. 3(a), 3(c), 3(e)] the fringe field structure in the SIA dominated regime ($\tau = \pi/2$) reflects the radial symmetry of the circulating current in this regime, and the fields are generated by concentric current loops with current flowing in opposite directions. The BIA term induces angular anistropy in the field distribution [Figs. 3(b), 3(d), 3(f)] providing a direct signature of the SOC ratio.
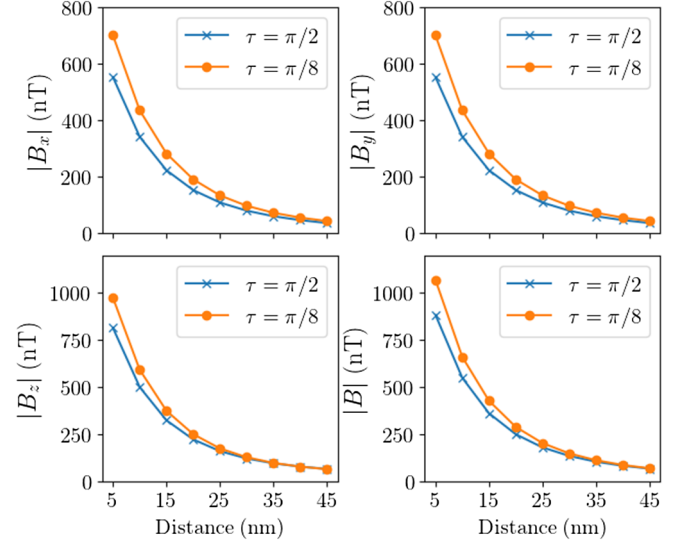
The magnitude of the orbital fringe field depends on the distance measured from the QW, e.g., decreasing fourfold at a distance of 20 nm from the InAs QW with respect to the field magnitude at the surface (Fig. 4), thus the close proximity achievable by nanoscale scanning probes can obtain even stronger responses within its sensitivity range. By adjusting the Fermi energy the magnitude of the fringe field can be increased but also compresses the orbital features through λ_{so}. The higher magnitude shown for currents with both SIA and BIA terms (crosses and blue lines in Fig. 4) occurs from higher currents due to the SOC-induced focusing effects. Furthermore, choices of different materials may lead to more detectable effects. Table I lists a variety of materials with either stronger magnetic fields or larger-scale spatial features, along with some more challenging materials that would have both (i.e., BiSb). The factors d_{fac} and B_{fac} are the scaling factors that should multiply the results shown for InAs (for which these are unity) to obtain the distances and field strengths for the other materials. For example, for BiSb the length scale of the features is $2.5 \times$ bigger and the fields generated are $4.6 \times$ bigger. In Table I we keep the two-dimensional electron density fixed to be 4×10^{11} cm^{-2}, and note that the features can also become larger (or smaller) for different electron densities.

The circulating dissipationless current associated with a single spin in a 2DEG formed in noncentrosymmetric materials with SOC creates spatial features highly sensitive to the underlying tunable spin-orbit field and the defect-spin direction, a reminiscent of the anisotropic dispersion relation and Friedel oscillations. Nanoscale scanning probe magnetometry, or potentially electron

ptychography, is sufficiently sensitive to measure the spatially resolved orbital contribution to the magnetic moment of a single spin. Sensitivities for NV sensors are better than 250 pT/Hz$^{1/2}$ [52–54] in ensembles, and 1.3 nT/Hz$^{1/2}$ for single NVs [55–58]. For a 10 kHz bandwidth, associated with a spin coherence time of 100 μs, the single-NV sensitivities are thus comparable to 100 nT. Thus the features predicted in Figs. 3 and 4, which include many features larger than 100 nT, are well within the sensitivity range even for coherent spins. For stable spins a sensitivity of 4.6 nT with spatial sensitivity of ∼50 nm [56] suggests direct imaging of the features is possible. Although the interaction strength mediated by these currents is much smaller than the RKKY interaction [41], coupling is still possible through the magnetic dipole to spins that have weak or absent exchange interaction such as f electrons or nuclear spins. The spatial structure of the defect magnetic moment affects its coupling to nearby rapidly oscillating fields from, e.g., nuclear spins, with implications for spin dynamics and coherent control of single spin states [59].

---

*adonaicruz@quantcad.com
Present address: QuantCAD LLC, 5235 S Harper Ct, Chicago, Illinois 60615, USA.
†michaelflatte@quantumsci.net

[1] B. E. Kane, A silicon-based nuclear spin quantum computer, Nature (London) **393**, 133 (1998).

[2] D. Loss and D. P. DiVincenzo, Quantum computation with quantum dots, Phys. Rev. A **57**, 120 (1998).

[3] *Semiconductor Spintronics and Quantum Computation*, edited by D. D. Awschalom, N. Samarth, and D. Loss (Springer Verlag, Heidelberg, 2002).

[4] K. Ichimura, A simple frequency-domain quantum computer with ions in a crystal coupled to a cavity mode, Opt. Commun. **196**, 119 (2001).

[5] G. Wolfowicz, F. J. Heremans, C. P. Anderson, S. Kanai, H. Seo, A. Gali, G. Galli, and D. D. Awschalom, Quantum guidelines for solid-state spin defects, Nat. Rev. Mater. **6**, 906 (2021).

[6] T. Matsui, Chr. Meyer, L. Sacharow, J. Wiebe, and R. Wiesendanger, Electronic states of Fe atoms and chains on InAs(110) from scanning tunneling spectroscopy, Phys. Rev. B **75**, 165405 (2007).

[7] D. H. Lee and J. A. Gupta, Tunable field control over the binding energy of single dopants by a charged vacancy in GaAs, Science **330**, 1807 (2010).

[8] R. C. Myers, M. H. Mikkelsen, J.-M. Tang, A. C. Gossard, M. E. Flatté, and D. D. Awschalom, Zero-field optical manipulation of magnetic ions in semiconductors, Nat. Mater. **7**, 203 (2008).

[9] T. Gaebel, M. Domhan, I. Popa, C. Wittmann, P. Neumann, F. Jelezko, J. R. Rabeau, N. Stavrias, A. D. Greentree, S. Prawer, J. Meijer, J. Twamley, P. R. Hemmer, and J. Wrachtrup, Room-temperature coherent coupling of single spins in diamond, Nat. Phys. **2**, 408 (2016).

[10] G. D. Fuchs, G. Burkard, P. V. Klimov, and D. D. Awschalom, A quantum memory intrinsic to single nitrogen–vacancy centres in diamond, Nat. Phys. **7**, 789 (2011).

[11] E. Togan, Y. Chu, A. S. Trifonov, L. Jiang, J. Maze, L. Childress, M. V. G. Dutt, A. S. Sørensen, P. R. Hemmer, A. S. Zibrov, and M. D. Lukin, Quantum entanglement between an optical photon and a solid-state spin qubit, Nature (London) **466**, 730 (2010).

[12] Y. Kato, R. C. Myers, D. C. Driscoll, A. C. Gossard, J. Levy, and D. D. Awschalom, Gigahertz electron spin manipulation using voltage-controlled g-tensor modulation, Science **299**, 1201 (2003).

[13] J. Pingenot, C. E. Pryor, and M. E. Flatté, Method for full Bloch sphere control of a localized spin via a single electrical gate, Appl. Phys. Lett. **92**, 222502 (2008).

[14] J. Pingenot, C. E. Pryor, and M. E. Flatté, Electric-field manipulation of the Landé g tensor of a hole in an $In_{0.5}Ga_{0.5}As$/GaAs self-assembled quantum dot, Phys. Rev. B **84**, 195403 (2011).

[15] M. D. Schroer, K. D. Petersson, M. Jung, and J. R. Petta, Field Tuning the g Factor in InAs Nanowire Double Quantum Dots, Phys. Rev. Lett. **107**, 176811 (2011).

[16] S. Takahashi, R. S. Deacon, A. Oiwa, K. Shibata, K. Hirakawa, and S. Tarucha, Electrically tunable three-dimensional g-factor anisotropy in single InAs self-assembled quantum dots, Phys. Rev. B **87**, 161302(R) (2013).

[17] N. Ares, G. Katsaros, V. N. Golovach, J. J. Zhang, A. Prager, L. I. Glazman, O. G. Schmidt, and S. De Franceschi, SiGe quantum dots for fast hole spin Rabi oscillations, Appl. Phys. Lett. **103**, 263113 (2013).

[18] A. Crippa, R. Maurand, L. Bourdet, D. Kotekar-Patil, A. Amisse, X. Jehl, M. Sanquer, R. Laviéville, H. Bohuslavskyi, L. Hutin, S. Barraud, M. Vinet, Y.-M. Niquet, and S. De Franceschi, Electrical Spin Driving by g-Matrix Modulation in Spin-Orbit Qubits, Phys. Rev. Lett. **120**, 137702 (2018).

[19] A. Ferrón, S. A. Rodríguez, S. S. Gómez, J. L. Lado, and J. Fernández-Rossier, Single spin resonance driven by electric modulation of the g-factor anisotropy, Phys. Rev. Res. **1**, 033185 (2019).

[20] M. W. Doherty, N. B. Manson, P. Delaney, F. Jelezko, J. Wrachtrup, and L. C. L. Hollenberg, The nitrogen-vacancy colour centre in diamond, Phys. Rep. **528**, 1 (2013).

[21] M. S. Grinolds, S. Hong, P. Maletinsky, L. Luan, M. D. Lukin, R. L. Walsworth, and A. Yacoby, Nanoscale magnetic imaging of a single electron spin under ambient conditions, Nat. Phys. **9**, 215 (2013).

[22] F. Casola, T. van der Sar, and A. Yacoby, Probing condensed matter physics with magnetometry based on nitrogen-vacancy centres in diamond, Nat. Rev. Mater. **3**, 17088 (2018).

[23] C. L. Degen, F. Reinhard, and P. Cappellaro, Quantum sensing, Rev. Mod. Phys. **89**, 035002 (2017).

[24] M. Noguchi, K. Hirakawa, and T. Ikoma, Intrinsic Electron Accumulation Layers on Reconstructed Clean InAs(100) Surfaces, Phys. Rev. Lett. **66**, 2243 (1991).

[25] G. R. Bell, T. S. Jones, and C. F. McConville, Accumulation layer profiles at InAs polar surfaces, Appl. Phys. Lett. **71**, 3688 (1997).

[26] L. Canali, J. W. G. Wildöer, O. Kerkhof, and L. P. Kouwenhoven, Low-temperature STM on InAs(110) accumulation surfaces, Appl. Phys. A **66,** S113 (1998).

[27] A. Fête, S. Gariglio, C. Berthod, D. Li, D. Stornaiuolo, M. Gabay, and J.-M. Triscone, Large modulation of the Shubnikov-de Haas oscillations by the Rashba interaction at the $LaAlO_3/SrTiO_3$ interface, New J. Phys. **16,** 112002 (2014).

[28] S. Singh and A. H. Romero, Giant tunable Rashba spin splitting in a two-dimensional BiSb monolayer and in BiSb/AlN heterostructures, Phys. Rev. B **95,** 165444 (2017).

[29] Q.-F. Yao, J. Cai, W.-Y. Tong, S.-J. Gong, J.-Q. Wang, X. Wan, C.-G. Duan, and J. H. Chu, Manipulation of the large Rashba spin splitting in polar two-dimensional transition-metal dichalcogenides, Phys. Rev. B **95,** 165401 (2017).

[30] Q. Liu, Y. Guo, and A. J. Freeman, Tunable Rashba effect in two-dimensional $LaOBiS_2$ films: Ultrathin candidates for spin field effect transistors, Nano Lett. **13,** 5264 (2013).

[31] J. Friedel, Metallic alloys, Nuovo Cimento **7,** 287 (1958).

[32] S. Lounis, A. Bringer, and S. Blügel, Magnetic Adatom Induced Skyrmion-Like Spin Texture in Surface Electron Waves, Phys. Rev. Lett. **108,** 207202 (2012).

[33] F. Freimuth, S. Blügel, and Y. Mokrousov, Relation of the Dzyaloshinskii-Moriya interaction to spin currents and to the spin-orbit field, Phys. Rev. B **96,** 054403 (2017).

[34] M. A. Ruderman and C. Kittel, Indirect exchange coupling of nuclear magnetic moments by conduction electrons, Phys. Rev. **96,** 99 (1954).

[35] T. Kasuya, A theory of metallic ferro- and antiferromagnetism on Zener's Model, Prog. Theor. Phys. **16,** 45 (1956).

[36] K. Yosida, Magnetic properties of Cu-Mn alloys, Phys. Rev. **106,** 893 (1957).

[37] S. Chesi and D. Loss, RKKY interaction in a disordered two-dimensional electron gas with Rashba and Dresselhaus spin-orbit couplings, Phys. Rev. B **82,** 165303 (2010).

[38] Z. Chen, Y. Jiang, Y.-T. Shao, M. E. Holtz, M. Odstrčil, M. Guizar-Sicairos, I. Hanke, S. Ganschow, D. G. Schlom, and D. A. Muller, Electron ptychography achieves atomic-resolution limits set by lattice vibrations, Science **372,** 826 (2021).

[39] G. Dresselhaus, Spin-orbit coupling effects in zinc blende structures, Phys. Rev. **100,** 580 (1955).

[40] Yu A. Bychkov and E. I. Rashba, Oscillatory effects and the magnetic susceptibility of carriers in inversion layers, J. Phys. C **17,** 6039 (1984).

[41] See Supplemental Material at http://link.aps.org/supplemental/10.1103/PhysRevLett.131.086301 for a detailed derivation of the current operator, the gradients of the Green's functions, the effective spin-orbit vector potentials, the symmetries of the circulating current, and a comparison with the RKKY interaction (also including Ref. [42]).

[42] H. Irie, T. Akiho, and K. Muraki, Determination of g-factor in InAs two-dimensional electron system by capacitance spectroscopy, Appl. Phys. Express **12,** 063004 (2019).

[43] D. H. Berman and M. E. Flatté, Electron-Beam Formation from Spin-Orbit Interactions in Zinc-Blende Semiconductor Quantum Wells, Phys. Rev. Lett. **105,** 157202 (2010).

[44] G. A. Fiete and E. J. Heller, *Colloquium:* Theory of quantum corrals and quantum mirages, Rev. Mod. Phys. **75,** 933 (2003).

[45] D. Grundler, Large Rashba Splitting in InAs Quantum Wells due to Electron Wave Function Penetration into the Barrier Layers, Phys. Rev. Lett. **84,** 6074 (2000).

[46] J. Yu, X. Zeng, S. Cheng, Y. Chen, Y. Liu, Y. Lai, Q. Zheng, and J. Ren, Tuning of Rashba/Dresselhaus spin splittings by inserting ultra-thin InAs layers at interfaces in insulating GaAs/AlGaAs quantum wells, Nanoscale Res. Lett. **11,** 477 (2016).

[47] J. Nitta, T. Akazaki, H. Takayanagi, and T. Enoki, Gate Control of Spin-Orbit Interaction in an Inverted $In_{0.53}Ga_{0.47}As/In_{0.52}Al_{0.48}As$ Heterostructure, Phys. Rev. Lett. **78,** 1335 (1997).

[48] P. Jamdagni, R. Pandey, and K. Tankeshwar, First principles study of Janus WSeTe monolayer and its application in photocatalytic water splitting, Nanotechnology **33,** 025703 (2022).

[49] J. Bouaziz, M. dos Santos Dias, F. Souza Mendes Guimarães, S. Blügel, and S. Lounis, Impurity-induced orbital magnetization in a Rashba electron gas, Phys. Rev. B **98,** 125420 (2018).

[50] B. A. Bernevig, J. Orenstein, and S.-C. Zhang, Exact SU(2) Symmetry and Persistent Spin Helix in a Spin-Orbit Coupled System, Phys. Rev. Lett. **97,** 236601 (2006).

[51] J. D. Jackson, *Classical Electrodynamics*, 3rd ed. (Wiley, New York, 1999).

[52] K. Jensen, N. Leefer, A. Jarmola, Y. Dumeige, V. M. Acosta, P. Kehayias, B. Patton, and D. Budker, Cavity-Enhanced Room-Temperature Magnetometry Using Absorption by Nitrogen-Vacancy Centers in Diamond, Phys. Rev. Lett. **112,** 160802 (2014).

[53] H. Zheng, J. Xu, G. Z. Iwata, T. Lenz, J. Michl, B. Yavkin, K. Nakamura, H. Sumiya, T. Ohshima, J. Isoya, J. Wrachtrup, A. Wickenbrock, and D. Budker, Zero-Field Magnetometry Based on Nitrogen-Vacancy Ensembles in Diamond, Phys. Rev. Appl. **11,** 064068 (2019).

[54] T. Wolf, P. Neumann, K. Nakamura, H. Sumiya, T. Ohshima, J. Isoya, and J. Wrachtrup, Subpicotesla Diamond Magnetometry, Phys. Rev. X **5,** 041001 (2015); **13,** 029903E (2023).

[55] D. A. Hopper, J. D. Lauigan, T.-Y. Huang, and L. C. Bassett, Real-Time Charge Initialization of Diamond Nitrogen-Vacancy Centers for Enhanced Spin Readout, Phys. Rev. Appl. **13,** 024016 (2020).

[56] M. L. Palm, W. S. Huxter, P. Welter, S. Ernst, P. J. Scheidegger, S. Diesch, K. Chang, P. Rickhaus, T. Taniguchi, K. Wantanabe, K. Ensslin, and C. L. Degen, Imaging of Submicroampere Currents in Bilayer Graphene Using a Scanning Diamond Magnetometer, Phys. Rev. Appl. **17,** 054008 (2022).

[57] W. S. Huxter, M. L. Palm, M. L. Davis, P. Welter, C.-H. Lambert, M. Trassin, and C. L. Degen, Scanning gradiometry with a single spin quantum magnetometer, Nat. Commun. **13,** 3761 (2022).

[58] E. Marchiori, L. Ceccarelli, N. Rossi, L. Lorenzelli, C. L. Degen, and M. Poggio, Nanoscale magnetic field imaging for 2D materials, Nat. Rev. Phys. **4,** 49 (2022).

[59] J. van Bree, A. Yu. Silov, P. M. Koenraad, and M. E. Flatté, Spin-Orbit-Induced Circulating Currents in a Semiconductor Nanostructure, Phys. Rev. Lett. **112,** 187201 (2014).